Journal of Materials Chemistry C

Accepted Manuscript

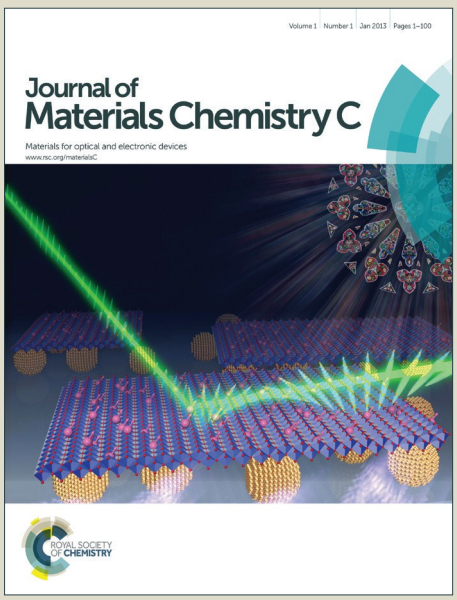

ROYAL SOCIETY OF CHEMISTRY

www.rsc.org/materialsC

Journal Name

ARTICLE

Multifunctional Near-Infrared Emitting Cr^{3+}-doped $Mg_4Ga_8Ge_2O_{20}$ Particles with Long Persistent, Photostimulated Persistent Luminescence and Photochromism Properties

Received 00th January 20xx,
Accepted 00th January 20xx

DOI: 10.1039/x0xx00000x

www.rsc.org/

Yahong Jin,[a] Yihua Hu,*[a] Lifang Yuan,[b] Li Chen,[a] Haoyi Wu,[a] Guifang Ju,[a] He Duan,[a] and Zhongfei Mu[a]

Here we report a series of multifunctional Cr^{3+}-doped magnesium gallogermanate particles. Several minutes of ultraviolet (UV) light activation can lead to strong near-infrared (NIR) long persistent luminescence (LPL) at 600–850 nm with a long lasting time at least 25 h. After the disappearance of LPL, NIR photostimulated persistent luminescence (PSPL) can be rejuvenated repeatedly for several times by external photo stimulus (visible or NIR light). Meanwhile, the material shows photochromism (PC) properties, *i.e.*, the surface color can change reversibly between white/pale green and ronbrown with high fatigue resistance by alternating UV and visible light irradiation. As the evaluated temperature to 300 ℃, the induced ronbrown surface color also can be bleached. This new multifunctional material has potential applications in widespread fields, such as *in vivo* bio-imaging, optical information write-in and read-out media, erasable optical memory media and optical sensors. The continuous traps distribution and modification were characterized. The optimum trap depth is determined to be 0.51-0.86 eV. In addition, we got insight into the multifunctional properties mechanism and the inner connections between them.

1. Introduction

In today's world, due to continuous growth in population and rapid development of industrialization, human beings face an unprecedented challenge that the global demand for more energy consumption seems to be ever increasing. Apart from developing new alternative energy sources, to make the most efficient use of energy is the first and foremost thing. Therefore, it is essential to push the development of sustainable and versatile optical storage and conversion materials. Multifunctional materials that absorb and convert certain types of energy, i.e. electromagnetic radiation, temperature, into light emission, or respond sensitively to the external stimulus, have attracted more and more interest for their widespread applications.

LPL, as a well known energy absorption-storage-releasing phenomenon, has stimulated extensive research interest for a long history.[1, 2] In past, the researchers in this field made great progress and gained a lot of substantial achievements. Before 2011, intensive researches were focused on the exploration of novel materials with LPL in visible light region and the studying of the complicated mechanism behind the LPL. Some developed long persistent phosphors (LPPs) have been put into commercial use in various fields, including security signs, night-vision panels and surveillance, decoration, imaging or optical memory storage media, etc., and some models for illustration the LPL mechanism have been proposed.[3-6] Until 2011, Pan *et al.* reported a trivalent chromium-doped gallogermanate system showing remarkable NIR LPL, which arouses a shockwave and opens the door to the design and fabrication of new type of persistent phosphors. Owing to the long persistent emission in the "tissue-transparent window" (～650-1000 nm) and the superiority of eliminating tissue autofluorescence, NIR LPPs enable them ideal as advanced biophotonic materials. State-of-the-art studies on NIR LPPs have extended their applications from daily life to biomedical fields, i.e., *in vivo* optical imaging and diagnosis.[7-10] Up to now, the generation of LPL in most of LPPs relies on short-wavelength excitation (e.g., ultraviolet light) which required rather limited tissue-penetration depth, and the NIR LPL from LPPs pre-charged in vitro will be waken continuously with decay time becoming extinguished when the electrons in suitable traps are released. Some storage materials also can be stimulated to release the electrons in deep traps by using a suitable illumination with low-energy light (such as NIR 980 nm and visible light). The photostimulated luminescence that can persist for long periods of time once the external energy is sufficient to push the electrons in deep traps to shallow traps is called PSPL.[11-13] By inducing PSPL, LPL can be revived repeatedly for several times, which can solve the

[a]*School of Physics and Optoelectronic Engineering, Guangdong University of Technology, WaiHuan Xi Road, No.100, Guangzhou 510006, China.*Email : huyh@gdut.edu.cn; Fax: +86 20 39322265; Tel: +86 20 39322262;*
[b]*Shenzhen Institutes of Advanced Technology, Chinese Academy of Sciences,1068 Xueyuan Avenue, Shenzhen 518055, PR China.*
† Footnotes relating to the title and/or authors should appear here.
Electronic Supplementary Information (ESI) available: [details of any supplementary information available should be included here]. See DOI: 10.1039/x0xx00000x

problem in NIR LPL materials mentioned above. In addition, this kind of storage materials can find their potential applications such as in optical information write-in and read-out, erasable and rewritable optical memory media.[13]

Upon external light stimulus, some substances change their surface color, which is referred to PC. It can be classified into two types: T-type (the induced surface color can be eliminated or regains the original state by a heat treatment) and P-type PC (the induced color can change reversely to the initial level under illumination at a specific wavelength). Though the intriguing PC phenomenon has been discovered more than 100 years and PC in organic materials have witnessed a booming development,[14-17] PC in inorganic powder materials are still in the early research stage.[28-23] Compared with organic counterparts, controllable macroscopic shape molding and high stability of inorganic PC materials enhance the applicability of this kind of smart material. Inspired by the light-driven and smart photo-switchable properties, inorganic PC materials have potential applications in various fields, including rewritable copy papers, ultrahigh-density optical information storage media, optical switches, logic gates, optic/electronic devices, and optical sensors.[15, 16, 18-20, 22] Different from that in organic PC materials, we find that the origin of PC in inorganic materials is usually closely related to energy storage and photochromic centers without structural change or isomerization. Also, the effective study on PC mechanism is still lacking.[18] The exploration of novel multifunctional materials to meet application requirements in different fields is of great practical value. In addition, owing to the aforementioned possible common feature among LPL, PSPL and PC properties, multidisciplinary measurements are helpful to reveal the detailed information about trap nature from the fundamental physical and chemical view, i.e., what is the trap center/ PC center, how do the traps distribute in the host and how to modify the traps distribution by external stimuli, and the electrons/holes motion processes.

Herein, we report the preparation of a series of Cr^{3+}-doped $Mg_4Ga_8Ge_2O_{20}$ (MGG) particles. The newly developed storage materials, exhibiting multifunctional properties including NIR persistent luminescence with a duration ＞25 h, PSPL in the NIR region with recyclable write-in and read-out performance, and reversible T/P- type PC with long life time (more than 3 months) in dark and high fatigue resistance, have potential applications in in vivo bio-imaging, erasable optical memory storage and optical switches. Moreover, based on the experimental results, we have comprehensively revealed the trap distributions and electron motion kinetics between adjacent traps in host lattice, which provides insights into the distinction and inner connections among NIR PL, LPL, PSPL and PC characteristics.

2. Experimental

2.1 Materials synthesis

The non-and Cr^{3+}-doped $Mg_4Ga_8Ge_2O_{20}$ Particles were all prepared via a high temperature solid-state reaction method. All starting reagents MgO (99.99%), Ga_2O_3 (99.99%), GeO_2 (99.99%), Cr_2O_3 (99.95%) and H_3BO_3 (99.5%) were used as received without further purification. Stoichiometric amount of raw materials were weighted according to the nominal composition of $Mg_4Ga_{8-x}Ge_2O_{20}:xCr^{3+}$ (x=0-0.02) with 3 mol% boric acid was used as flux. Firstly, the raw materials except H_3BO_3 were dried at 120 ℃ for 5 h. After this, individual batches were mixed and milled homogeneously in an agate mortar. The resultant mixtures were heated up to 1100 ℃, held for 2 h in ambient atmosphere, and then cooled down to room temperature naturally with the furnace. After intermediately ground to improve the homogeneity, the mixtures were sintered at 1400 ℃ for 6 h in air atmosphere. Finally, they were furnace-cooled to room temperature and ground evenly for subsequent measurements.

2.2. Measurements and characterization

Phase identification of all the as-prepared samples were performed by using a Panalytical X'pert Pro diffractometer at room temperature using Cu Kα irradiation with a power of 40 kV at 40 mA. The X-ray diffraction data for Rietveld structure analysis were collected over the 2θ range from 10 to 120°in a step-mode with interval step of 0.02°. The steady-state PL and photoluminescence excitation (PLE) spectra were characterized by a high-resolution FLS980 fluorescence spectrophotometer (Edinburgh Instruments Ltd., UK) with the photomultiplier tube operating at 400 V using a 450 W Xe-lamp as excitation source. The LPL spectra, photostimulated luminescence spectra, photostimulated persistent luminescence (PSPL) including write-in and read-out curves were recorded by a Hitachi F-7000 fluorescence spectrophotometer (Tokyo, Japan) equipped with a Xe lamp (150 W) as excitation source at 400 V working voltage. LPL decay curves were collected immediately by a GFZF-2A single-photon counter system after the samples were irradiated by 254 nm. High temperature PL spectra were measured from room temperature to 300 ℃ by the FLS980 fluorescence spectrophotometer combined with a high temperature setup (Tianjin Orient-KOJI). Appropriate optical filters were used to avoid the appearance of stray light in all spectral measurements. Diffuse reflectance spectra (DRS) of all obtained powder samples were measured by an UV-2450 spectrophotometer (Shimadzu UV-2450, Japan) using $BaSO_4$ as a reference. High temperature DRS were measured after the samples were heated up to the objective temperature, held for 1 min in a homemade heating setup and then cooled down to room temperature. Thermoluminescence (TL) glow curves and LPL excitation spectra were recorded with a FJ-427A1 thermoluminescence meter (Beijing, China). Unless otherwise specified, prior to the measurement, the samples were pre-heated at 400 ℃ for 1 min to completely eliminate the charge carriers in traps. After cooling down to room temperature, they were pre-irradiated by the required wavelength light for 5 min, then put in dark for a given time and finally measured at a linear heating rate of 1 ℃/s in the temperature range of 25-400 ℃. Some measurements are carried out with a preheating at different desired temperatures (50-320 ℃) for 10 s using the homemade heating setup after the samples were exposed to a specified irradiation. ESR spectra were obtained with an X-band JES FA200 electron paramagnetic resonance spectrometer at a frequency 9.50 GHz under the microwave power of 0.998 mW at 77 K in vacuum before and after the samples were irradiated by different wavelength light.

3. Results and discussion

3.1 Phase identification and crystal structure

The X-ray diffraction (XRD) pattern of the as-prepared MGG is in

agreement with the JCPDS 42-0238 (Fig. S1(a)). The crystal structure of MGG was solved and refined from powder XRD data in the triclinic space group $P\bar{1}$ with cell parameters a=8.832212 Å, b=9.794205 Å, c=10.280132 Å. Fig. 1(a) shows the structural overview of the MGG host lattice. It is highly condensed by rigid framework of corner-sharing between octahedrons/tetrahedrons GaO_6/GaO_4 and tetrahedrons GeO_4 with channels filled by Mg (Fig. S1(b)). To validate the Cr^{3+}-doing in host lattice and triclinic structure model, Rietveld method was used to make a theoretical calculation based on powder XRD data MGG:0.001Cr (Fig. 1(b)). The refinement results are listed in Table S1, indicating that a small amount of Cr^{3+} as dopant can be neglected for structure determination and Cr^{3+} ions tend to occupy seven Ga^{3+} sites those are six-coordinated rather than other four-coordinated Ga^{3+} or Ge^{4+} sites.

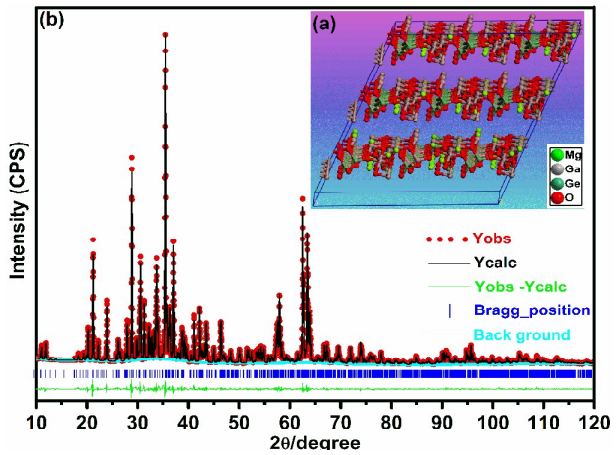

Fig. 1 (a) Crystal structure of MGG. (b) Experimental (red dotes) and calculated (black solid line) XRD patterns and the different between them (green solid line) for the MGG:0.001Cr. The blue ticks mark the Bragg reflection positions and the cyan line represents back ground.

3.2 Photoluminescence properties of MGG and MGG:Cr particles

Fig. 2(a) shows the excitation and emission spectra of the undoped MGG powder. The excitation spectrum monitored at 460 nm exhibits a broad band ranging from 200 to 300 nm with the maximum at 260 nm, which is probably caused by the transition from the valence band to the conduction band of the MGG host.[24, 25] Under excitation at 260 nm, the material exhibits a broadening emission band extending from ~300 to ~700 nm with the maximum at 460 nm. The self-activation emission center originates from the Ga-O transition of regular octahedral site.[26-32] Fig. 2(b) shows excitation spectrum of MGG: Cr powder monitored at 693 nm. It covers a very broad spectral region (between 200 and 620 nm) and consists of four main excitation bands. Obviously, the strong excitation band at 260 nm is ascribed to the MGG host excitation. Compared to the host excitation in Fig. 2(a), the excitation in the wavelength range from 200 to 350 nm is broadened due to the appearance of weak shoulder excitation band in the edge region of the host excitation (~280 nm) originating from the $^4A_2 \rightarrow {}^4T_1(^4P)$ transition of Cr^{3+} ions. The other two excitation bands centered at 410 nm ($^4A_2 \rightarrow {}^4T_1(^4F)$ transition) and 580 nm ($^4A_2 \rightarrow {}^4T_2(^4F)$ transition) are also assigned to the 3d intra-shell transitions of Cr^{3+} ions. It is noted that the excitation spectrum of phosphor MGG: Cr strongly overlaps with the MGG host emission, indicating the possibility of energy transfer (ET) from host to Cr^{3+} ions. Under different excitations, MGG: Cr yields the similar emission in near-infrared region (Fig. S2(a)). As shown in Fig. 2(c), excitation of MGG: xCr (x=0-0.02) phosphors at 260 nm gives two predominated broad emission bands. One is MGG host emission (460 nm). Another broad emission band extending from ~650 to ~850 nm, which is probably caused by the spin-allowed $^4T_2 \rightarrow {}^4A_2$ transitions from some disordered Cr^{3+} ions in the gallogermanate system, was superimposed with two narrow zero phonon lines observed at 693 and 714 nm. They are labeled as R and N_2 which correspond to the spin-forbidden $^2E \rightarrow {}^4A_2$ transitions of Cr^{3+} occupying the ideal and much distorted octahedral sites (caused by an antisite defects $Ga_{Mg}^{\bullet} / Mg_{Ga}^{'}$ located in the first cationic neighbors of Cr^{3+} or more defects clustered around, respectively.[33-38] At low temperature (77 K, inset of Fig. 2(c)), the splitting of the ^2E level into ^2E ($2\bar{A}$) and ^2E ($\bar{E}$) doublets (R_1 and R_2) differing from that at room temperature is resolved. The dependence of emission intensity at 460 and 693 nm on the Cr^{3+} doping concentration is plotted in Fig. S2(b). The host emission decreases continuously ending with disappearance as the Cr^{3+} doping concentration increases from 0.05% to 2%, further proving the above conclusion that energy transfers from host to Cr^{3+} ions, which is also demonstrated by the decreasing lifetime of host emission (Fig. S2(c)). Meanwhile, the Cr^{3+} emission intensity increases, reaching the maximum at x=0.0025, and then decreases, which is due to concentration quenching.[39]

Impressively, the simultaneous presence of $^2E \rightarrow {}^4A_2$ and $^4T_2 \rightarrow {}^4A_2$ transitions suggests that Cr^{3+} in MGG host locates in an intermediate crystal field site, i.e., the ^2E level of Cr^{3+} ion is close to the $^4T_2$ level ($D_q/B \approx 2.3$). Otherwise, Cr^{3+} in strong crystal field gives rise to sharp line emissions and in weak crystal field leads to a broadband emission. The character of the Cr^{3+} emission depends on the crystal field strength (D_q). According to the Tanabe and Sugano diagram (Fig. S2(d)), the ratio (D_q/B) between D_q and the Racah parameter B reflects the criterion for evaluation of the crystal field suffered by Cr^{3+} in host lattice.[40-43] The values of D_q and B of Cr^{3+} in octahedral symmetry can be estimated utilizing spectroscopic data by the following equations (1) and (2).[44]

$$10D_q = \nu_1 \quad (1)$$

$$B = (2\nu_1^2 + \nu_2^2 - 3\nu_1\nu_2) / (15\nu_2 - 27\nu_1) \quad (2)$$

where ν_1 and ν_2 correspond to band energies of $^4A_2 \rightarrow {}^4T_2$ (^4F) and $^4A_2 \rightarrow {}^4T_1$ (^4F) transitions, respectively. The values of D_q and B are calculated to be about 1724 cm^{-1} and 724 cm^{-1}, respectively. Whereas, the estimated ratio of D_q/B (~2.38) confirms the deduction above. Unexpectedly, the Cr^{3+}-doped MGG (a typical sample MGG: 0.0025Cr for an example is shown in Fig. 2(d)) exhibits noticeable different emission spectra upon excitations at different wavelengths (260-400 nm). With the longer wavelength excitation,

the emission intensity of $^4T_2 \rightarrow {}^4A_2$ transitions becomes dominated, which may be attributed the perturbation of the localized traps.

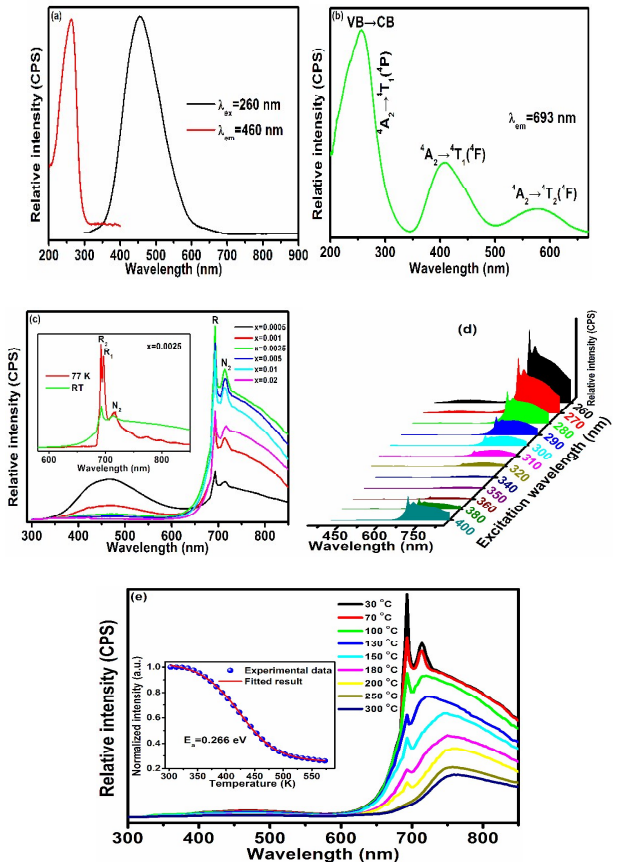

Fig. 2 (a) Excitation (red curve, monitored emission at 460 nm) and emission (black curve, excitation at 260 nm) spectra of the undoped MGG particle. (b) Excitation spectra of Cr^{3+}-doped MGG particle at the emission of 693 nm. (c) Emission spectra of Cr^{3+}-doped MGG particle by the excitation of 260 nm. Inset: the emission spectra of MGG:0.0025Cr^{3+} at room temperature and 77 K for comparison. (d) Emission spectra of MGG:0.0025Cr^{3+} particle under the excitations with different wavelengths (260-400 nm). (e) Temperature dependent emission spectra of MGG:0.0025Cr^{3+} excited at 260 nm. Inset: the corresponding thermal quenching profile (the blue dots are experimental data and the red curve represents the fitted result according to equation 3).

The temperature-dependent emission spectra of MGGO: Cr^{3+} have been measured from 30 up to 300 ℃ in steps of 10 ℃ and some selected emission spectra are shown in Fig. 2(e). Note that not only the intensity but also the profiles of the emission spectra change significantly as the temperature increases. The decreasing emission intensity is caused by thermal quenching effect with a large amount of nonradiative transitions in Cr^{3+} ions. A smooth thermal quenching profile for MGGO: Cr^{3+} is given (inset of Fig. 2(e)) through fitting with a simple single-barrier model (3).[45-47]

$$I_T = I_0[1+(\Gamma_0/\Gamma_v)\exp(-\frac{E_a}{kT})]^{-1} \quad (3)$$

where I_T is the emission intensity, Γ_0 is the attempt rate in the nonradiative process, Γ_v is the radiative rate, k is the Boltzmann constant, T is the temperature (K) and E_a is the activation energy.

With temperature increasing, the emission corresponding to $^4T_2 \rightarrow {}^4A_2$ radiative transition gradually becomes more efficient than that of $^2E \rightarrow {}^4A_2$ transitions, resulting in the disappearance of narrow lines ($^2E \rightarrow {}^4A_2$) and domination by the broad $^4T_2 \rightarrow {}^4A_2$ band. This observation may be explained from two aspects in view of optical pumping and thermal expansion of unit-cell at high temperature. Normally, the transition $^2E \rightarrow {}^4A_2$, being both spin and parity forbidden, is rather longer lived than that of $^4T_2 \rightarrow {}^4A_2$. As the temperature is increased, both emission intensities decrease, but the emission of the $^4T_2 \rightarrow {}^4A_2$ band decreases much slower and shows a slight red-shift. Due to the small energy level difference between ^2E and $^4T_2$ levels, there a possibility that the thermal quenching from $^4T_2$ level is partly compensated by the progressive thermal population of electrons in $^4T_2$ level which is fed from ^2E level. In addition, the intensity ratio between narrow and broadband emission from Cr^{3+} ion depends strongly on the energy separation between ^2E and $^4T_2$ levels governed by crystal field. The MGG unit-cell will expand to some extent with the increase of temperature, which causes the crystal field splitting decrease as Cr^{3+}-O^{2-} bond length increases. Consequently, the decrease of the corresponding energy level of $^4T_2$, accompanying with the almost invariant ^2E level which is insensitive to vibrational modulation, leads to the gradually dominated broad band emission and slight red-shift of band position.[43, 48, 49]

3.3 Long persistent luminescence properties of MGG and MGG:Cr particles

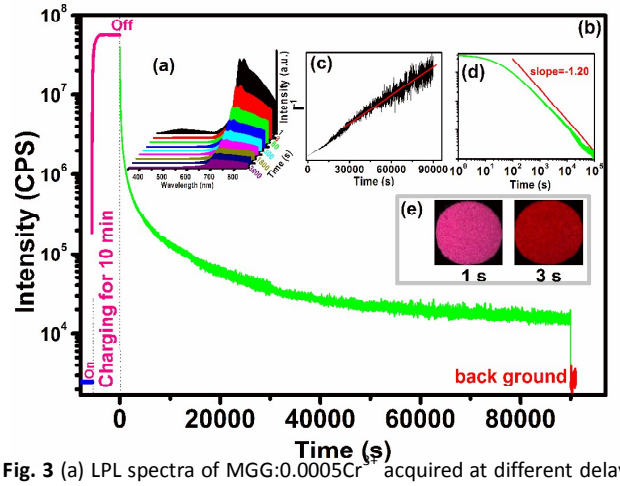

Fig. 3 (a) LPL spectra of MGG:0.0005Cr^{3+} acquired at different delay times (1-3600 s). (b) LPL decay curve monitored at 693 nm after 10 min charging process by 280 nm in a linear-logarithmic diagram. (c) The reciprocal NIR LPL intensity (I^{-1}) as a function versus decay time (t) and the fitted result (red line) in time range of t=~23000-90000 s. (d) The LPL decay curve is plotted in double-logarithmic diagram. (e) Digital images of MGG:0.0005Cr^{3+} particle 1 s (left) and 3 s (right) after 280 nm irradiation.

After UV light irradiation, the as-synthesized MGG and MGG:Cr exhibit long persistent luminescence with blue and NIR emission, respectively. To further understand the effectiveness of different excitation wavelengths for NIR LPL, the relationship between LPL intensity ($I_{15\ s}$, recorded 15 s after the removal of the excitation source to avoid the possible large deviation in the initial stage of fast decay) monitored at 693 nm and the excitation wavelengths over the spectral range of 200–600 nm is plotted in Fig. S3. It is clearly seen that NIR LPL can be induced by a wide range of excitation wavelengths (200-400 nm, defined as NIR LPL excitation spectra) and the most effective excitation wavelength is ~280 nm. Compared with the PL excitation spectrum (Fig. 2(b)), it can be drawn that NIR LPL of MGG:Cr sample can not be achieved under visible light (400–700nm) illumination though the excitation light within this wavelength range is effective in inducing the NIR PL emission. The NIR LPL only can be effectively achieved under UV irradiation (200-360 nm), indicating that the electrons storage in electron traps in this material may be responsible for the generation of LPL.[18] LPL decay curves recorded at 693 nm emission for MGG:xCr^{3+} (x=0-0.02) LPPs after the stoppage of the irradiation by 280 nm are shown in Fig. S4. The optimal doping concentration of Cr^{3+} for LPL is determined to be about 0.05%, which is much lower than that for PL. After 10 min irradiation by 280 nm, the LPL spectra of MGG: 0.0005Cr^{3+} acquired at different delay times during the first 1 h are given in Fig. 3(a). It is obvious that the LPL spectrum is initially (1-3 s) composed of two parts, i.e., host and Cr^{3+} emissions in blue and NIR region, and then quickly changes to the NIR emission alone. This change is intuitively reflected by the LPL photos of MGG: 0.0005Cr taken at different decay times (Fig. 3(e)) and confirms ET from host to Cr^{3+} ions. The profiles of LPL spectra (t $>$3 s) almost keep invariant with decay time, indicating that the NIR LPL originates from the Cr^{3+} emitting centers. Compared with the emission spectra (Fig. 2(c)), the most noticeable difference lies in the sharp decrease of R/N_2 emission ratio, similar to that for Cr^{3+}-doped $ZnGa_2O_4$.[34, 35, 38] It confirms that two distinct types of Cr^{3+} surrounding environment are presented within the host lattice and suggests that the nearby antisite defects are postulated to play a specific role in the generation of LPL.[50] As shown in Fig. 3(b), when exciting MGG:0.0005Cr LPP by 280 nm, one can observe that it undergoes a rapid charging process, reaching a constant value with 10 min excitation, and then shows a LPL decay curve after the ending of the excitation. LPL decay curve, manifested as a function of LPL intensity versus decay time (t), contains a very fast decay process at the beginning and then a slow decay process. Even after 25 h, the high LPL intensity is still detected, inferring that NIR LPL can last much longer than 25 h, which enables that MGG:Cr phosphor may be potential to be used in long-term *in vivo* bioimaging. The duration (>25 h) was also taken for an eye with the aid of a night vision monocular in dark. Fig. 3(c) also shows the reciprocal LPL intensity (I^{-1}) as a function versus decay time (t). The I^{-1}-t curve in the time period of 7-25 h can be well fitted by a linear function: $I^{-1}\times10^{6}=1.44t+7.88\times10^{-4}$, indicating that a tunneling-related process is involved in NIR LPL,[51, 52] which will be discussed in detail later. An exponential decay profile followed by a straight line in a semi-logarithmic plot would be observed for a single trap with first order kinetics. It is obvious not the case. Higher order kinetics for LPL decay will show a line with a slope of $b/(1-b)$ in a double-logarithmic plot according to $I_t = I_0 / [(1+t/\tau)^{b/(b-1)}]$.[53] Fig. 3(d) displays that a straight line with the slope of -1.20 after 3 h decay can be obtained, implying a high kinetic order of b=6. However, the expected retrapping can not be observed in TL experiments (see in TL analysis), suggesting the presence of a trap distribution in MGG:Cr.

3.4 Photostimulated persistent luminescence of MGG:Cr particles

LPL phenomenon can be observed when we illuminate the UV pre-irradiated MGG:Cr phosphors with a 980 nm laser.[11, 12, 54] In other words, the energy stored in the MGG:Cr phosphor can be released gradually in the form of NIR emission by NIR light stimulation, such as a 980 nm NIR laser, resulting in NIR PSPL. Visually, the nearly extinguished NIR LPL after a long decay time is rejuvenated again and looks like much brighter. In this regard, MGG: 0.0005Cr phosphor, pre-charged by 280 nm for 10 min with 24 h decay, is stimulated with 980 nm light for 30 s. PSPL spectrum (Fig. S5(a)), recorded at 5 s after the turning off the stimulation light, is similar to that of the LPL spectrum in Fig. 3(a). It infers that the generation of PSPL and LPL is identical after the captured electrons are photostimulated from deep to shallow traps. Electron traps are redistributed under photostimulation. With this concept in mind, the PSPL decay curve (monitored at 693 nm) is also collected and displayed in Fig. S5(b). It is significant that the 980 nm light illumination induces a notable increase of the LPL intensity and thus triggers a new LPL phenomenon. In addition, the NIR PSPL could be also repeatedly revived with some what a lower intensity after subsequent 980 nm NIR light stimulation at every interval, indicating that electrons in deep traps are released batch by batch at each time of photostimulation. The NIR PSPL induced by using incoherent biotissue-penetrable NIR light (980 nm) enables multiplex detection modes in optical bio-imaging either *in situ* or *ex situ*.

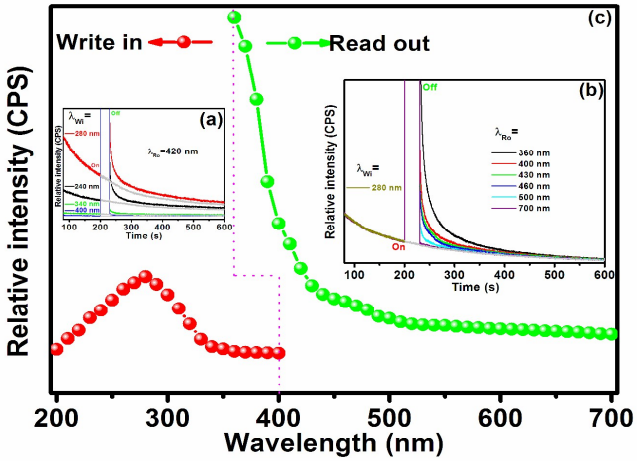

Fig. 4 (a) LPL decay curves monitored at 693 nm with (colored solid lines) and without (gray solid lines) external light stimulus (420 nm) after excitations with different wavelengths (200-400 nm). (b) LPL decay curves monitored at 693 nm with (colored solid lines) and without (gray solid lines) external light stimuli (360-700 nm) after excitation by 280 nm. In both cases (a) and (b), the photostimulation starts at 200 s after the removal of excitations with a duration time of 30 s. (c) PSPL write-in (red ball curve) and read-out (green ball curve) spectra derived from (a) and (b), respectively.

Due to the photostimulable property, MGG:Cr can find its

potential applications as a new type of readable, erasable and rewritable optical memory media in optical information storage field. Thus, the energy ranges of write-in and read-out required for the generation of NIR PSPL should be determined. To obtain write-in spectrum of PSPL, MGG: 0.0005Cr phosphor was pre-irradiated for 10 min using monochromatic UV light from 200 to 400 nm with a step of 10 nm, followed by none or 420 nm light stimulation for 30 s (Fig. 4(a)). Then, the LPL decay curves were recorded after the stoppage of 420 nm stimulation. PSPL intensity is derived from the difference between the LPL intensities of each set of decay curves recorded with and without additional photostimulation. The PSPL write-in spectrum is achieved by connecting the obtained data of PSPL intensities as a function of the write-in wavelengths (200–400 nm). Similarly, the PSPL read-out spectrum is acquired by setting the pre-charging wavelength at 280 nm for 10 min and changing the read-out wavelengths from 350 to 700 nm (Fig. 4(b)). Therefore, both of PSPL write-in and read-out spectra are obtained and shown in Fig. 4(c). Note that the most effective write-in wavelength (~ 280 nm) and the shape of PSPL write-in spectrum are almost in coincidence with that of the LPL excitation spectrum in Fig. S3. It is not an accident as it looks. Instead, it indicates the inner association between NIR LPL and PSPL that the filling of the deep traps under UV irradiation accompanied with the photoionization of Cr^{3+} ions forming photochromic centers plays a critical role in both cases. From the PSPL read-out spectrum, we can see that the stimulation irradiation in a wide wavelength range (360-700 nm) can gives birth to the PSPL. The irradiation light with shorter wavelength is much more effective to induce the PSPL. Though there is partial overlapping between the PSPL read-out and write-in spectra, the PSPL write-in intensity in the overlapping range between 360 and 400 nm is very weak to be ignored. So, it can be regarded that write-in and read-out spectra are completely separated without mutual interference between them, which is important for an erasable and rewritable optical memory device. Furthermore, the broad spectra of PSPL write-in and read-out widen the applicability and strengthen the suitability.

3.5 Reversible photochromism

Interestingly, upon UV light irradiation, the surface color of MGG:Cr powder changes quickly from white/pale green to ronbrown and then can be substantially bleached after it is exposed into sunlight or other artificial white light for several minutes. To qualitatively character the PC property, diffuse reflectance measurements on the MGG:Cr samples with and without UV irradiation are carried out. As shown in Fig. S6 (a)-(f), before light irradiation, samples show a body color change from white to pale green with increasing Cr^{3+} doping concentrations, which is due to the appearance of two stronger absorption bands of Cr^{3+} ions centered at ~ 410 and 580 nm in visible region. After irradiated by UV irradiation (280 nm), the MGG:Cr samples show an additional broad absorption wave band in light range from 300 to 800 nm by comparing with the non-irradiated samples. The presence of the dominated absorption band between 350 and 550 nm naturally result in the ronbrown surface color of UV-irradiated samples. To precisely evaluate the changing degree of PC, the contrast of the PC capability (CT) can be assessed by the ratio of reflectivity before [$R_{(uncolored)}$] and after [$R_{(colored)}$] UV-irradiation, *i.e.*, $CT=R_{(uncolored)}/R_{(colored)}$. Therefore, the CT curves of MGG:Cr samples are obtained and shown in Fig. 5. It is notable that the optimal doing concentration of Cr^{3+} for the best PC performance is determined to be 0.05% and the PC capability becomes lower with the increasing Cr^{3+} doping concentration, which are in agreement with that for the LPL. As reflected in the inset of Fig. 5, the reversible PC phenomenon (including coloration and bleaching processes) and the changing trend of PC capability mentioned above are clearly observed without leaving any permanent structural damage.

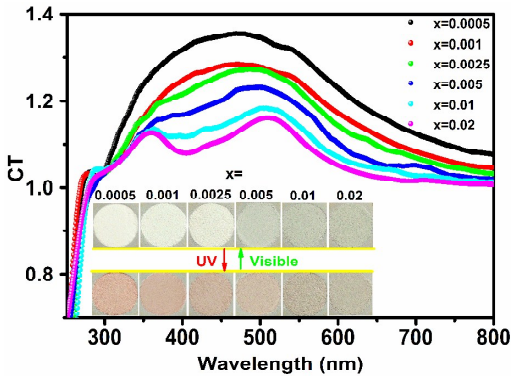

Fig. 5 CT curves of MGG: xCr (x=0.0005-0.02) samples plotted according to Fig. S6 (a)-(f). Inset: Digital photos of MGG: xCr (x=0.0005-0.02) samples by alternative exposing into UV (280 nm) and visible light.

As an reversible PC material, it is of important significance to study the coloring/bleaching spectra and photoresponse time of MGG:Cr powder. To reveal the coloring spectra, we plotted PC coloring spectra by measuring the DRS of MGG: 0.0005Cr sample with the pre-irradiation for 3 min using monochromatic UV light ranging from 200 to 400 nm. Where, the monochromatic UV light is achieved from a Xe lamp (150 W) by adjusting an optical grating. As shown in Fig. S7 (a), the DRS show dips of reflectivity (R%) varying in degree. The PC coloring spectrum was then obtained by plotting the values (1-R%) at 480 nm as a function of pre-irradiation light wavelength, as indicated in Fig. S7 (b). It can be easily found again that the PC coloring spectrum is identical in shape to the LPL excitation spectrum and PSPL write-in spectrum, indicating that either PC, LPL or PSPL phenomenon is controlled by the deep electron traps. Though the degree of the coloring/bleaching is directly proportional to the intensity of irradiation light, the photoresponse time of coloring in a specified condition can be roughly determined by the time separation between the beginning of light irradiation and the saturation of coloration. The diffuse reflectivity at 480 nm of MGG: 0.0005Cr decreases quickly at first and then gradually with longer pre-irradiation (280 nm) time, and approaches a saturation at about t=1 min (Fig. S7 (c)), manifesting a fast photoresponse and trap filling rate. In the same way, the fully colored MGG: 0.0005Cr sample was irradiated for 1 min using monochromatic light ranging from 300 to 700 nm and then the PC bleaching spectrum was obtained by plotting the values (R%) at 480 nm as a function of bleaching light wavelengths (Fig. S7 (d)). It can be found that in order to realize the decoloration, the effective

bleaching wavelength should be within near UV to visible region (360-600 nm), and the shorter the bleaching wavelength, the more effective the bleaching rate is. The light with wavelength shorter than 360 nm not only can bleach but also color the sample, which eventually reaches a dynamic equilibrium. The reversible PC behavior which was examined by monitoring the reflectivity values at 480 nm following alternative UV/visible light irradiation (10 cycles) is shown in Fig. S7 (e), indicating good repeatability in the coloration-bleaching processes. The reversible recording-erasing of information property enables this material to be used as optical switches or high density optical memories.[18, 19]

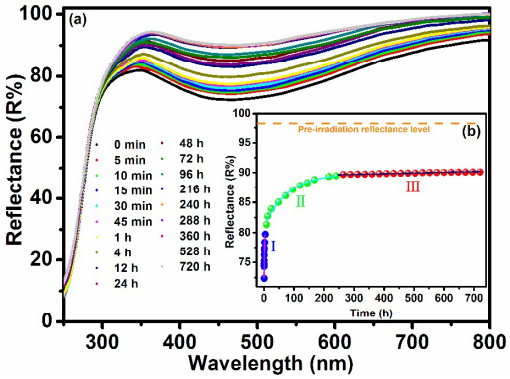

Fig. 6 DRS of sample MGG: 0.0005Cr over 720 h in dark at room temperature after the coloration by 280 nm for 3 min. (b) The dependence of DRS intensity at 480 nm on delay time according to the data in (a).

The UV light induced ronbrown surface color is long lived in dark at room temperature and still can be observed obviously 3 months later. The reflectance spectra of MGG: 0.0005Cr sample over 720 h after the initial coloration are shown in Fig. 6(a). The reflectivity at 480 nm, as presented in Fig. 6(b) increases with prolonged time containing three processes: the initially linear increment process (~0-25 h, process Ⅰ), the later gradual increment process (~25-250 h, process Ⅱ) and the last nearly stable state (~250-700 h, process Ⅲ). Naturally, it can be assumed that process Ⅰ is mainly associated to the LPL decay and dominated by shallower traps, process Ⅱ is accompanied by PSPL which is caused by deep traps and process Ⅲ is related to deeper traps from which the trapped electrons are hardly to be released at room temperature in the host lattice.

In addition to external stimulation through light illumination, the colored sample also can be quickly bleached by heating treatment at ~300 ℃. As shown in Fig. 7(a), the temperature-dependent (30-300 ℃) reflectance spectra of the pre-irradiated sample were measured. The reflectivity (R%) values at 480 nm were plotted as a function of rising temperatures (Fig. 7(b)), which indicates the occurrence of three different bleaching processes under thermal treatment. The thermal bleaching rate is low when the heating temperature is low (~30-60 ℃, process A), then becomes faster as the heating temperature increases (~60-190 ℃, process B) and finally turns to much slower at higher heating temperatures (~190-300 ℃, process C), which are reflected in Fig. 7(c). Process A originates from the escaping of electrons from the shallower traps. At high temperature, trapped electrons in both of shallower and deep traps can be released, resulting in faster bleaching rate in process B, which indicates that the maximal density of traps lies in the deep traps. However, the small number of trapped electrons in deeper traps leads to the slower bleaching rate in process C, albeit higher temperature beyond 190 ℃. The processes A, B and C firmly demonstrate the processes Ⅰ, Ⅱ and Ⅲ above, and prove the above assumption that three processes caused by traps with different depths.

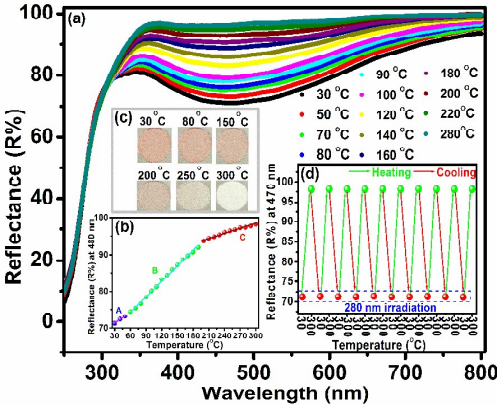

Fig. 7 (a) DRS of sample MGG: 0.0005Cr measured at an elevated temperature (30-300 ℃). (b) The dependence of DRS intensity at 480 nm on temperature according to the data from (a). (c) Digital photos of MGG: 0.0005Cr taken at different temperatures. (d) DRS intensity changes at 480 nm by alternating 280 nm irradiation for 3 min (after cooling down to room temperature) and heat treatment at 300 ℃ for 3 min.

3.6 Thermoluminescence

To further explicitly understand the generation and inner connections among PL, LPL, PSPL and PC properties in Cr^{3+}-doped MGG, detailed knowledge of the nature of traps in host lattice is therefore critical. At present, TL method is used as a powerful tool to obtain some valuable information about traps presented in a host, such as the trap depths, traps distribution, and more specifically on possible interactions between them including the trapping and de-trapping processes.[51, 53, 55-58] A comprehensive study to reveal the mechanisms which remain the subject of discussion was carried out by performing a series of TL experiments using combined approaches in the same run: *i.e.*, the measurements of traps filling, distribution, fading, and electrons motion between different traps upon excitation with selective excitation wavelengths and varying excitation duration at varying temperatures.

It is easy to image that the traps in the host can not be filled immediately when exciting the MGG: Cr powders. Instead, they are charged with a process and then reach saturation, namely, charging process. This process can be visually displayed by the TL curves recorded after the sample is irradiated with different excitation duration. Fig. 8(a) shows the TL curves recorded 1 min after the sample MGG: 0.0005Cr was pre-irradiated by UV light (280 nm) with varying excitation duration, *i.e.*, from 1 s to 10 min. The excited

electrons are intercepted quickly to fill deeper traps in priority to a degree and then the shallow traps. The TL intensity increases with longer excitation duration due to more traps are being filled, nearly reaching the maximum at t=1 min which is almost in agreement with the time that required in PC property (Fig. S7(c)). Before reaching the saturation, slight increase of TL intensity still can be observed as the excitation duration is prolonged to 5 min, which may be attributed to the trapped electrons from host excitation. Overall, the very broad non-structure TL band (30-350 ℃) and a shift of the TL maximum position towards lower temperatures infer that the trap system may be composed of multiple levels with continuous distributions rather than one or more straightforward discrete energy levels with simple first or second order kinetics. In this realistic case，the usually used models, i.e., first, second or even general order kinetics, which are derived under some ideal premises are in fact invalid and difficult to obtain accurate results with physical meaning.[59-64] The initial rise method which is independent on the The initial rise method which is independent on the order of kinetics is therefore adopted for estimating trap depths through equation (4).[6, 62, 65]

$$I_T = A\exp(-E_T / kT) \quad (4)$$

where, A is a constant, I_T is TL intensity, T represents temperature and E_T is required trap depth. When the TL glow curves are plotted as a function of ln(I_T) versus 1/T, a straight line for each TL curve at the low-temperature side can be obtained. As illustrated in Fig. 8(b), the estimation of E_T which can be easily read from the slope of the straight line varies from 0.376 to 0.241 eV. Though they reflect just the depths of very shallow traps at room temperature, the decreasing values of E_T confirm the initial filling of deep traps at the expense of filling the shallow traps and strongly demonstrate the presence of a continuous trap depth distribution.

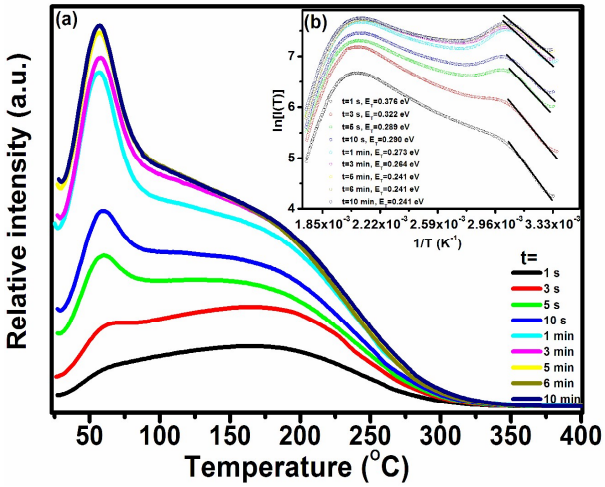

Fig. 8 TL glow curves of sample MGG: 0.0005Cr recorded after the 280 nm excitation with various durations (1 s-10 min). (b) Initial rise method analysis on the TL glow curves of sample MGG: 0.0005Cr as a function of excitation duration based on equation (4).

In principle, trap capacity can be measured by TL intensity. Fig. S8 exhibits the TL curves recorded 3 min after the all the obtained samples MGG: Cr were pre-irradiated by UV light (280 nm) for 5 min, indicating that the optimal Cr^{3+}-doping concentration for trap creation is approximately 0.05%. The value is the same as that for LPL (PSPL) and PC but much lower than that for the best PL (0.25%), confirming that LPL (PSPL) and PC properties are strongly related to traps. Moreover, a striking difference exists in concentration quenching mechanisms between PL and LPL (PSPL)/PC. The concentration quenching in LPL (PSPL) and PC is attributed to the interactions between the trapping centers with other vicinal defects. As the reduced distance between adjacent trap centers caused by increasing doping concentration, the interactions between them increase, which results in the observed concentration quenching phenomenon.

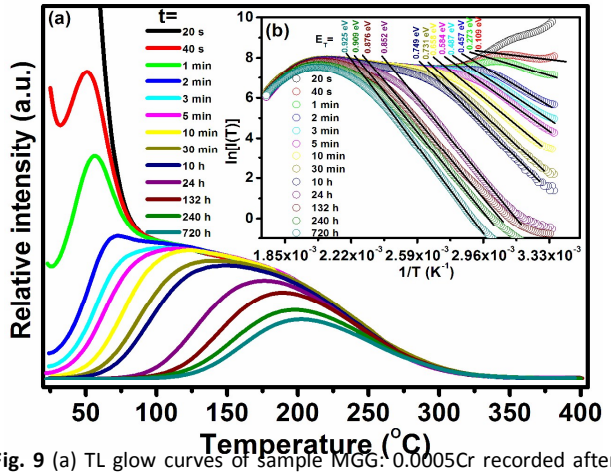

Fig. 9 (a) TL glow curves of sample MGG: 0.0005Cr recorded after the 280 nm excitation with various delay durations (20 s-720 h). (b) Initial rise method analysis on the TL glow curves of sample MGG: 0.0005Cr as a function of delay durations based on equation (4).

The presence of trap distribution also can be derived from TL fading curves. Also, it would be of great interest to figure out the fading processes which are responsible for the long lived LPL (PSPL) and PC. The TL fading curves of sample MGG: 0.0005Cr, where the waiting duration after the removal of UV excitation (280 nm) for 5 min is varied from 20 s to 720 h, are shown in Fig. 9(a). As expected, it is logical to observe that the extremely broad TL band recorded with longer delay time is narrower lacking the tail at low-temperature side and such a changing becomes much slower as the delay time is beyond 24 h, indicating that electrons captured in shallow traps are released much faster than that in deep traps at room temperature. The initial rise method was also applied to roughly study the trap depth changing with delay time. However, in this case, the TL curves should be corrected by the thermal quenching profile in inset of Fig. 2(e), otherwise the TL glow curve at higher temperature can be underestimated leading to the estimated results with a large deviation. As shown in Fig. 9(b), it is worthwhile to note that the gradual deepening of the trap depth (from 0.109 to 0.925 eV) with longer delay time verifies the existence of the continuous trap distribution in MGG: Cr.

To get deeper insight into and guarantee the accuracy of the trap depth distribution, it is meaningful to study the isothermal TL curves recorded after a short time preheating of the specimen at

varying temperatures.[66-68] Only then can the effect that the initial part of the higher temperature peak might be obscured by the tail of the low-temperature peak be partially avoided. Fig. 10(a) shows the partial-cleaning TL curves of UV (280 nm) pre-irradiated sample MGG: 0.0005Cr for 5 min recorded after 10 s preheating at a certain temperature (T_{stop}) at the beginning of the 3 min delay duration time and then cooling down to room temperature. Naturally, the low-temperature tail is diminished completely and quickly with, leaving the remaining filled deep traps from which the electron escaping requires much higher thermal energy. As a consequence, the continuous distribution of traps with lower depths is emptied to a certain deeper depth, depending on T_{stop}. The overlapping peaks presented in the broad TL band can be resolved by plotting the relationship of T_M-T_{stop} (T_M is the temperature at TL band maximum). From the inset in Fig. 10(a), one can note that T_M nearly shows a linear dependence on T_{stop} without any flat plateau, firmly confirming the presence of continuous distribution of traps rather than several distinguished individual peaks.[58, 62] So, the TL curves were studied by the initial rise method (Fig. S9) with the same procedure above. The estimated trap depths in the whole preheating temperature range within 30-240 ℃, beyond which the results would be unreliable due to the extremely weak intensity, were plotted in Fig. 10(b). According to the trap depth changing trend, three divisions can be divided, *i.e.*, 30-60 ℃, 60-180 ℃ and 180-240 ℃. Additionally, the LPL decay curves of the UV pre-irradiated sample MGG: 0.0005Cr recorded using the same method were shown in Fig. S10, suggesting that the traps distribution in higher temperature region (approximately >180 ℃) no longer makes contribution to LPL generation at room temperature. Thus, it can be concluded that the traps distributions between 60 and 180 ℃ with depths of 0.51-0.86 eV are suitable for room temperature LPL. The traps in lower, intermediate and higher temperature regions with trap depths of 0.48-0.51 eV, 0.51-0.86 eV and 0.51-0.92 eV control the processes Ⅰ, Ⅱ and Ⅲ (Fig. 6(b)), as well as processes A, B and C (Fig. 7(b)), respectively.

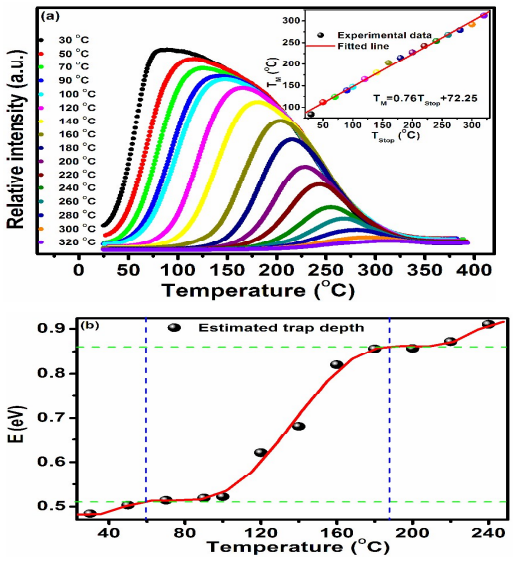

Fig. 10 TL glow curves of sample MGG: 0.0005Cr at different temperatures ranging from 30 to 320 ℃. Inset: the dependence of T_m on T_{stop} plotted according to the data from (a). (b) Estimated trap depths as a function of temperature.

Inversely, under light stimulus, the trapped electrons in deep traps can partially move back to shallow traps. To clearly understand the electrons motion processes, TL measurements were conducted on UV pre-irradiated MGG: 0.0005Cr powder undergoing 240 h delay time (in order to eliminate the electrons in shallow traps) with and without 480 nm light re-stimulation, as shown in Fig. S11(a). Notably, TL curve profile is significantly modified by 480 nm light stimulation, *i.e.*, the shallow traps are refilled while the deep traps are partially emptied and the TL band at maximum shows a shift to lower temperature. It indicates that some of the electrons in the deep traps can be photostimulated by external light stimulation and some of the released electrons can transfer to shallow traps, inducing the filling of the emptied shallow traps. This process is accompanied with the occurrence of faster LPL decay, PSPL and the bleaching of PC properties. The influence of changing the re-irradiation wavelength on the TL curves is given in Fig. S11(b). Stimulation light with shorter wavelength within 360-700 nm is more effective to force the electrons to escape from shallow and even deep traps.

3.7 Mechanism

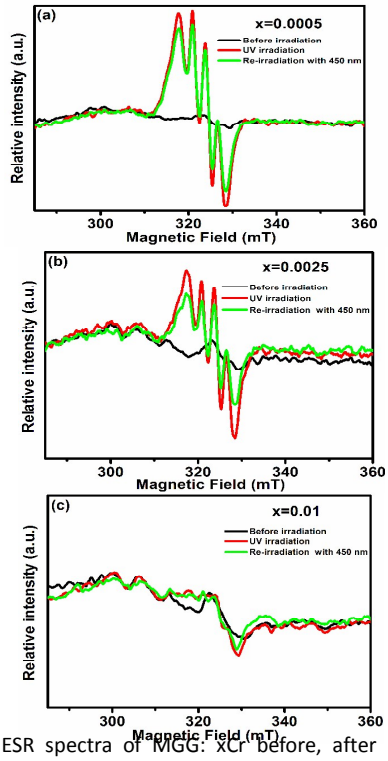

Fig. 11 (a) ESR spectra of MGG: xCr before, after UV (280 nm) irradiation and re-irradiation by 450 nm: (a) x=0.0005, (b) x=0.0025 and (c) x=0.01.

After UV light irradiation, the induced LPL (PSPL) and PC phenomena originate from the trapping of excited electrons by the traps accompanied with the formation of photochromic centers. Cr^{3+} ion plays an important role and can act as an effective probe in detecting the site distortion and valence state change. As a valid evidence, the electron spin resonance (ESR) spectra of pristine samples (x=0.0005, 0.0025 and 0.01) in Figure S12(a) show features

at g=5.13, 4.29, 2.38 and 1.97. The low magnetic field resonance signal at g=5.13 (the signal at g=4.29 is typically for the unwanted impurity Fe^{3+} ion)[69-71] is generally assigned to isolated Cr^{3+} ions in strongly distorted sites, whilst the high magnetic field resonance signals are also entirely attributed to isolated Cr^{3+} ions but in weakly distorted sites rather than the combination of isolated Cr^{3+} and exchange coupled Cr^{3+} pairs due to low doping concentration,[72-76] By *in situ* irradiating the samples with UV light, it is notable that the ESR spectra shown in Figure S12(b) emerge a sharp strong resonance signal at g=1.98 which originates from Cr^{5+} ions.[77-79] Under UV light irradiation, according to the formation processes of $Cr^{3+} \xrightarrow{h\nu} Cr^{4+} \xrightarrow{h\nu} Cr^{5+}$, some excited electrons from Cr^{3+} ions in MGG can be captured gradually by traps, leading to the generation of color centers Cr^{4+} and Cr^{5+}. The hyperfine structures of Cr^{5+} ESR spectra for the samples after *in situ* UV irradiation and reirradiation by visible light (~450 nm) are characterized by zoom scanning ESR spectra. As shown in Figures 11 (a), (b) and (c), the increasing and decreasing of ESR intensity correspond to reversible conversions of $Cr^{3+} \rightarrow Cr^{5+}$ and $Cr^{5+} \rightarrow Cr^{3+}$ by alternating UV and visible irradiation/thermal treatment, leading to the reversible coloring and bleaching processes. As the Cr^{3+} ion doping concentration increases, the ESR signal intensity of Cr^{5+} decreases, resulting in poorer PC performance (in Figure 5). It infers that electron traps play a critical role in the stabilization of high valence of chromium (Cr^{4+} and Cr^{5+}).

Based on the aforementioned results, a schematic energy level diagram for illustration the versatile properties in MGG: Cr particle is constructed (Fig. 12). Upon UV irradiation (260 nm), MGG host absorbs the incident photons and the electrons in valence band (VB) are pumped into conduction band (CB). Then, the excited electrons and holes more randomly in CB and VB, respectively, and blue emission is observed along with the combination of electrons and holes. Meanwhile, energy from MGG host can be effectively transferred to the Cr^{3+} ions due to strong spectral overlap between the MGG host emission and the excitation bands of Cr^{3+} ions (Fig. 2(a) and (b)), leading to the simultaneous NIR emission from Cr^{3+} ions. However, some electrons and holes can be trapped by native defects (such as oxygen, germanium and zinc vacancies) via nonradiative relaxation. After the stoppage of UV irradiation, the subsequent recombination of electrons and holes released gradually from these native traps induces the blue LPL. Likewise, the nonradiative persistent ET from MGG host to Cr^{3+} ions results in the excitation of the Cr^{3+} 3d electrons from the ground state to higher excited states ($^4T_2$, and $^4T_1$ (^4F)). Subsequently, most of excited electrons jump downward to lower energy levels ($^4T_2$ and ^2E) via nonradiative relaxation and then $^4A_2$ ground state, leading to NIR LPL. But some excited electrons in $^4T_1$ (^4F) level may be intercepted by the nearby electron traps through tunneling which causes the PC phenomenon. Under 280 nm excitation, Cr^{3+} is excited directly from ground state to $^4T_1$ (^4P) level. Similarly, besides the intrinsic NIR emission caused by the majority of excited electrons the residual excited electrons can be captured by electron traps along with the occurrence of PC. At room temperature, the captured electrons can be thermally released gradually returning back to $^4T_1$ (^4P) level through CB and transferring to $^4T_1$ (^4F) and $^4T_2$ levels via tunneling, giving rise to NIR LPL and gradual color bleaching. The light excitation with wavelength beyond 360 nm hardly induces these observations because that the energy is insufficient to promote the electrons to higher energy levels near/beyond the bottom of CB. Just for this reason, direction excitation from ground state to $^4T_1$ (^4P) level has the most capacity to fill the traps. Because of a large amount of localized traps (such as antisite defects) around $^4T_2$ level (Cr^{3+} ions in strong distorted sites), the broad PL corresponding to the $^4T_2$-$^4A_2$ transitions is assisted by the LPL, showing much stronger intensity (Fig. 2(d)). In addition, direction excitation of Cr^{3+} to the highest level gives birth to the most efficient NIR LPL and PC performance as well as the PSPL performance afterward. By external photo-stimulus or heating treatment, the traps distribution can be modulated that the captured electrons in deep traps are pushed to the empty shallow traps and then return to excited energy levels, causing NIR photostimulated luminescence, which greatly facilitates the bleaching processes. After the stoppage of the external stimulation, NIR PSPL is observed.

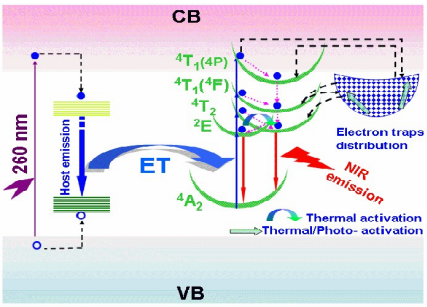

Fig. 12. Schematic illustration for the multifunctional properties in MGG: Cr. Blue filled circles hollow circles represent electron and holes, respectively. Black dashed lines mark the electron/hole motion and pink dotted lines represent nonradiative relaxation.

4. Conclusions

We have developed the synthesis and characterization of a series of Cr^{3+}-doped magnesium gallogermanate particles with multifunctional properties. The energy transfer from host to Cr^{3+} can be observed. After UV irradiation, the material exhibits an extremely NIR LPL (> 25h) for in biomedical use. By using the temperature elevated PL corrected TL, the suitable trap depths for LPL has been determined to be 0.51-0.86 eV. The regained NIR PSPL by external photo stimulus make the MGG: Cr promising act as an excellent imaging plate for optical information write-in and read-out. The smart reversible PC (white/pale green↔ronbrown) with high fatigue resistance by alternating UV and visible light irradiation enables the material to be used as erasable optical memory media, optical switches and sensors. Accordingly, the corresponding schematic diagram for illustration the multifunctional properties mechanism has been discussed in detail.

Acknowledgments

The authors acknowledge the financial support from the National Natural Science Foundation of China (no. 21471038); the Special Funds for University Discipline and Specialty Construction of Guangdong Province, China (No. 2013KJCX0066).

References

1. E. N. Harvey, *A history of luminescence from the earliest times until 1900*, American Philosophical Society, 1957.
2. J. Hölsä, *Electrochem. Soc. Interface*, 2009, **18**, 42-45.
3. T. Matsuzawa, Y. Aoki, N. Takeuchi and Y. Murayama, *J. Electrochem. Soc.*, 1996, **143**, 2670-2673.
4. H. Yamamoto and T. Matsuzawa, *J. Lumin.*, 1997, **72**, 287-289.
5. P. Dorenbos, *J. Electrochem. Soc.*, 2005, **152**, H107-H110.
6. T. Aitasalo, J. Hölsä, H. Jungner, M. Lastusaari and J. Niittykoski, *J. Phys. Chem. B*, 2006, **110**, 4589-4598.
7. Z. Pan, Y.-Y. Lu and F. Liu, *Nat. Mater.*, 2012, **11**, 58-63.
8. Z. Li, Y. Zhang, X. Wu, L. Huang, D. Li, W. Fan and G. Han, *J. Am. Chem. Soc.*, 2015, **137**, 5304-5307.
9. A. Abdukayum, J.-T. Chen, Q. Zhao and X.-P. Yan, *J. Am. Chem. Soc.*, 2013, **135**, 14125-14133.
10. Y. Li, S. Zhou, Y. Li, K. Sharafudeen, Z. Ma, G. Dong, M. Peng, and J. Q, *J. Mater. Chem. C*, 2014, **2**, 2657-2663.
11. F. Liu, W. Yan, Y.-J. Chuang, Z. Zhen, J. Xie and Z. Pan, *Sci. Rep.*, 2013, **3**, 1544.
12. Y. Jin, Y. Hu, L. Chen, Y. Fu, Z. Mu, T. Wang and J. Lin, *J. Alloy. Compd.*, 2014, **616**, 159-165.
13. H. v. Seggern, *Braz. J. Phys.*, 1999, **29**, 254-268.
14. L. Chalkley, *Chem. Rev.*, 1929, **6**, 217-280.
15. J. Zhang, Q. Zou and H. Tian, *Adv. Mater.*, 2013, **25**, 378-399.
16. A. Bianco, S. Perissinotto, M. Garbugli, G. Lanzani and C. Bertarelli, *Laser Photonics Rev.*, 2011, **5**, 711-736.
17. J. Yao, K. Hashimoto and A. Fujishima, *Nature*, 1992, **355**, 624-626.
18. Y. Jin, Y. Hu, Y. Fu, L. Chen, G. Ju and Z. Mu, *J. Mater. Chem. C*, 2015, **3**, 9435-9443.
19. M. Akiyama, *Appl. Phys. Lett.*, 2010, **97**, 1905.
20. S. Kamimura, H. Yamada and C.-N. Xu, *Appl. Phys. Lett.*, 2013, **102**, 031110.
21. Y. Jin, Y. Hu, Y. Fu, Z. Mu and G. Ju, *Mater. Lett.*, 2014, **134**, 187-189.
22. J. Ueda, T. Shinoda and S. Tanabe, *Opt. Mater. Express*, 2013, **3**, 787-793.
23. G. Ju, Y. Hu, L. Chen and X. Wang, *J. Photoch. Photobio. A*, 2013, **251**, 100-105.
24. G. Gao and L. Wondraczek, *J. Mater. Chem. C*, 2013, **1**, 1952-1958.
25. J. Kim, H. Kang, W. Kim, J. Kim, J. Choi, H. Park, G. Kim, T. Kim, Y. Hwang and S. Mho, *Appl. Phys. Lett.*, 2003, **82**, 2029-2031.
26. S.-h. Wu and H.-C. Cheng, *J. Electrochem. Soc.*, 2004, **151**, H159-H163.
27. S. Y. Bae, J. Lee, H. Jung, J. Park and J.-P. Ahn, *J. Am. Chem. Soc.*, 2005, **127**, 10802-10803.
28. Z. Gu, F. Liu, X. Li, J. Howe, J. Xu, Y. Zhao and Z. Pan, *J. Phys. Chem. Lett.*, 2009, **1**, 354-357.
29. L. Zou, X. Xiang, M. Wei, F. Li and D. G. Evans, *Inorg. Chem.*, 2008, **47**, 1361-1369.
30. J. Kim, H. Park, C. Chon, H. Moon and T. Kim, *Solid State Commun.*, 2004, **129**, 163-167.
31. Y. Zhang, Z. Wu, D. Geng, X. Kang, M. Shang, X. Li, H. Lian, Z. Cheng and J. Lin, *Adv. Funct. Mater.*, 2014, **24**, 6581-6593.
32. L. Xu, Y. Su, Q. Zhou, S. Li, Y. Chen and Y. Feng, *Cryst. Growth Des.*, 2007, **7**, 810-814.
33. D. Chen, Y. Chen, H. Lu and Z. Ji, *Inorg. Chem.*, 2014, **53**, 8638-8645.
34. M. Allix, S. b. Chenu, E. Véron, T. Poumeyrol, E. A. Kouadri-Boudjelthia, S. Alahrache, F. Porcher, D. Massiot and F. Fayon, *Chem. Mater.*, 2013, **25**, 1600-1606.
35. A. Bessière, S. Jacquart, K. Priolkar, A. Lecointre, B. Viana and D. Gourier, *Opt. Express*, 2011, **19**, 10131-10137.
36. Y. Zhuang, J. Ueda and S. Tanabe, *Appl. Phys. Express*, 2013, **6**, 052602.
37. N. Basavaraju, S. Sharma, A. Bessiere, B. Viana, D. Gourier and K. R. Priolkar, *J. Phys. D: Appl. Phys.*, 2013, **46,** 375401.
38. A. Bessière, S. K. Sharma, N. Basavaraju, K. R. Priolkar, L. Binet, B. Viana, A. J. Bos, T. Maldiney, C. Richard and D. Scherman, *Chem. Mater.*, 2014, **26**, 1365-1373.
39. D. Dexter and J. H. Schulman, *J. Chem. Phys.*, 1954, **22**, 1063-1070.
40. Y. Tanabe and S. Sugano, *J. Phys. Soc. Jan.*, 1954, **9**, 766-779.
41. I. Nikolov, X. Mateos, F. Güell, J. Massons, V. Nikolov and P. Peshev, *Opt. Mater.*, 2004, **25**, 53-58.
42. B. Struve and G. Huber, *Appl. Phys. B*, 1985, **36**, 195-201.
43. K. Ogasawara, F. Alluqmani and H. Nagoshi, *ECS J. Solid State Sc.*, 2016, **5**, R3191-R3196.
44. J. R. Perumareddi, *Coord. Chem. Rev.*, 1969, **4**, 73-105.
45. Y.-T. Tsai, C.-Y. Chiang, W. Zhou, J.-F. Lee, H.-S. Sheu and R.-S. Liu, *J. Am. Chem. Soc.*, 2015, **137**, 8936-8939.
46. P. Dorenbos, *J. Phys.: Condens. Matter*, 2005, **17**, 8103.
47. J. Ueda, P. Dorenbos, A. J. Bos, A. Meijerink and S. Tanabe, *J. Phys. Chem. C*, 2015, **119**, 25003-25008.
48. J. Hehir, M. Henry, J. Larkin and G. Imbusch, *J. Phys. C Solid State Phys.*, 1974, **7**, 2241.
49. B. Henderson, A. Marshall, M. Yamaga, K. O'Donnell and B. Cockayne, *J. Phys. C Solid State Phys.*, 1988, **21**, 6187.
50. A. De Vos, K. Lejaeghere, D. E. P. Vanpoucke, J. J. Joos, P. F. Smet and K. Hemelsoet, *Inorg. Chem.*, 2016, **55**, 2402-2412.
51. J. Trojan-Piegza, J. Niittykoski, J. Hölsä and E. Zych, *Chem. Mater.*, 2008, **20**, 2252-2261.
52. Y. Jin, Y. Hu, Y. Fu, G. Ju, Z. Mu, R. Chen, J. Lin and Z. Wang, *J. Am. Ceram. Soc.*, 2015, **98**, 1555-1561.
53. K. Van den Eeckhout, A. J. Bos, D. Poelman and P. F. Smet, *Phys. Rev. B*, 2013, **87**, 045126.
54. D. C. Rodriguez Burbano and E. Martín Rodríguez, *J. Mater. Chem. C*, 2014, **2**, 228-231.
55. J. Botterman, J. J. Joos and P. F. Smet, *Phys. Rev. B*, 2014, **90**, 085147.
56. J. Trojan-Piegza, E. Zych, J. Hölsä and J. Niittykoski, *J. Phys. Chem. C*, 2009, **113**, 20493-20498.

57. D. Kulesza and E. Zych, *J. Phys. Chem. C*, 2013, **117**, 26921-26928.
58. Y. Jin, Y. Fu, Y. Hu, L. Chen, G. Ju and Z. Mu, *Opt. Mater. Express*, 2015, **5**, 1488-1497.
59. J. Randall and M. Wilkins, *Proc. R. Soc. A*, 1945, **184**, 390-407.
60. J. Randall and M. Wilkins, *Proc. R. Soc. A,* 1945, **184**, 366-389.
61. R. Chen and S. W. McKeever, *Theory of thermoluminescence and related phenomena*, World Scientific, 1997.
62. S. W. McKeever, *Thermoluminescence of solids*, Cambridge University Press, 1988.
63. A. Bos, *Radiat. Meas.*, 2006, **41**, S45-S56.
64. R. Chen, S. McKeever and S. Durrani, *Phys. Rev. B*, 1981, **24**, 4931.
65. V. Pagonis, G. Kētēs, G. Kitis and C. Furetta, *Numerical and practical exercises in thermoluminescence*, Springer Science & Business Media, 2006.
66. K. Kato, I. Tsutai, T. Kamimura, F. Kaneko, K. Shinbo, M. Ohta and T. Kawakami, *J. Lumin.*, 1999, **82**, 213-220.
67. P. Kivits and H. Hagebeuk, *J. Lumin.*, 1977, **15**, 1-27.
68. A. Vedda, M. Nikl, M. Fasoli, E. Mihokova, J. Pejchal, M. Dusek, G. Ren, C. Stanek, K. McClellan and D. Byler, *Phys. Rev. B*, 2008, **78**, 195123.
69. F. Li, K. M. Van Heuvelen, K. K. Meier, E. Münck and L. Que Jr, *J. Am. Chem. Soc.*, 2013, **135**, 10198-10201.
70. M. P. Hendrich, D. Petasis, D. M. Arciero and A. B. Hooper, *J. Am. Chem. Soc.*, 2001, **123**, 2997-3005.
71. A. Aboukaïs, E. Zhilinskaya, I. Filimonov, N. Nesterenko, S. Timoshin and I. Ivanova, *Catal. Lett.*, 2006, **111**, 97-102.
72. S. Drew, J. Pilbrow, P. Newman and D. MacFarlane, *J. Phys. D: Appl. Phys.*, 2001, **34**, 2987.
73. A. Murali and J. L. Rao, *J. Phys.: Condens. Matter*, 1999, **11**, 1321.
74. M. Haouari, H. B. Ouada, H. Maaref, H. Hommel and A. Legrand, *J.Phys.: Condens. Matter*, 1997, **9**, 6711.
75. D. Gourier, A. Bessière, S. K. Sharma, L. Binet, B. Viana, N. Basavaraju and K. R. Priolkar, *J. Phys. Chem. Solids*, 2014, **75**, 826-837.
76. N. Basavaraju, K. R. Priolkar, D. Gourier, S. K. Sharma, A. Bessièr and B. Viana, *Phys. Chem. Chem. Phys.*, 2015, **17**, 1790-1799.
77. L. Zhang and P. A. Lay, *J. Am. Chem. Soc.*, 1996, **118**, 12624-12637.
78. C. Kesavulu, R. Chakradhar and C. Jayasankar, *J. Mol. Struct.*, 2010, **975**, 93-99.
79. H. Schneider, K. Ikeda, B. Saruhan and H. Rager, *J. Eur. Ceram. Soc.*, 1996, **16**, 211-215

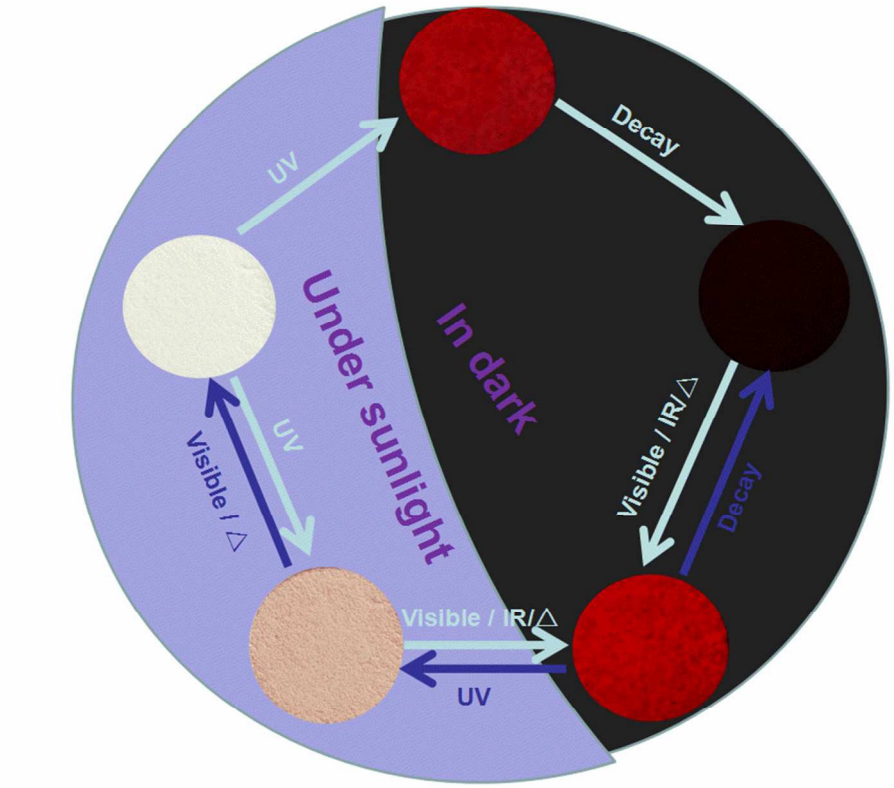

81x70mm (300 x 300 DPI)